



Cite this: *Dalton Trans.*, 2017, **46**,
3906

Received 31st January 2017,
Accepted 22nd February 2017

DOI: 10.1039/c7dt00381a

rscl.li/dalton

Vacancy and anti-site disorder scattering in AgBiSe₂ thermoelectrics†

Felix Böcher, Sean P. Culver, Jan Peilstöcker, Kai S. Weldert and Wolfgang G. Zeier*

AgBiSe₂ has recently been shown to exhibit promising thermoelectric properties due to the low intrinsic thermal conductivity, stemming from a large degree of lattice anharmonicity. While samples synthesized *via* solid-state routes usually exhibit n-type behavior, p-type transport is seen in samples based on solution synthetic routes possibly due to Ag vacancies. Using a combined approach of synchrotron diffraction, thermoelectric transport measurements and thermal transport modeling, we show the influence of synthetically induced Ag vacancies on the structure of AgBiSe₂ and the thermoelectric transport. We identify the degree of anti-site disorder of Ag and Bi due to the occurring phase transformation and the influence of the vacancy content on metal ordering. Additionally, we show that anti-site disorder and vacancies act as scattering centers for phonons, leading to enhanced point defect scattering in this interesting thermoelectric material.

1. Introduction

Thermoelectric materials convert heat into electricity and are therefore a promising approach for waste heat recovery in general. Important materials parameters for a good thermoelectric efficiency are a high thermopower (or Seebeck coefficient) S , a good electrical conductivity σ and a low thermal conductivity κ , leading to a materials figure of merit $zT = \frac{S^2 \sigma}{\kappa} T$ at the temperature T . The electrical conductivity and thermopower are highly dependent on the carrier concentration,^{1,2} therefore a common approach is to find materials with very low intrinsic thermal conductivities³ and optimize the carrier densities *via* doping in order to maximize the figure of merit.

Recently, AgBiSe₂ has attracted interest as a potential thermoelectric material due to the intrinsically low thermal conductivity, stemming from a high Grüneisen parameter and strong phonon–phonon interactions.⁴ While AgBiSe₂ exhibits a low thermal conductivity, optimization of the carrier concentration is necessary and different doping strategies have been shown to be successful for this intrinsically n-type doped material. For instance, substitution of Ag with Nb or Bi with Pb has led to promising figures of merit,⁵ as well as aliovalent doping on the anion site with AgBiSe_{2-x}X_x (X = Cl, Br, I).⁶ However, there are still some open questions about the intrinsic nature of charge carriers. While solid-state syntheses lead

to intrinsic n-type behavior,^{5,6} solution syntheses lead to holes as charge carriers.^{7,8} This is especially important, as the p-type material has been predicted to perform well due to a beneficial carrier pocket anisotropy.⁹ The observed p-type transport in the solution-based route was believed to stem from Ag vacancies, which would act as hole dopants in AgBiSe₂.⁸

As defects *via* vacancy doping and intrinsic vacancies have been shown to be very influential on thermoelectric transport^{10–12} in a variety of Zintl compounds,^{13,14} Cu chalcogenides,¹⁵ half-Heuslers¹⁶ as well as SnTe,^{17,18} here we explore the influence of the synthetic variation of the Ag content on the structural and thermoelectric transport properties. A combination of synchrotron diffraction, thermoelectric transport measurements and modeling of point defect scattering was used to elucidate the influence of defects on transport in AgBiSe₂. All Ag_{1-x}BiSe₂ synthesized *via* solid-state reactions are intrinsically electron conducting and a crossover to p-type behavior cannot be observed. Synchrotron diffraction shows significant anti-site disorder between Ag and Bi, which decreases with increasing the amount of Ag vacancies. The anti-site disorder and the vacancies act as phonon scattering centers, severely affecting the lattice thermal conductivity. This work shows the importance of considering the defect chemistry and disorder in thermoelectric materials and illustrates the influence of defects on transport.

2. Experimental methods

Synthesis

Bulk samples of polycrystalline Ag_{1-x}BiSe₂ ($x = 0, 0.01, 0.02, 0.05, 0.07$) were prepared by solid-state reactions using elemen-

Institute of Physical Chemistry, Justus-Liebig-University Giessen, Heinrich-Buff-Ring 17, D-35392 Giessen, Germany. E-mail: wolfgang.g.zeier@phys.chemie.uni-giessen.de

† Electronic supplementary information (ESI) available: The crystallographic data of Ag_{1-x}BiSe₂ obtained using Rietveld refinements of X-ray Bragg scattering. See DOI: 10.1039/c7dt00381a

tal powders of Ag (Alfa Aesar, 99.999%), Bi (Chempur, 99.999%) and Se (Alfa Aesar, 99.999%). The phase purity of the starting elements was verified by X-ray diffraction and all synthetic procedures were carried out in an Ar glovebox. In order to ensure completely dry conditions, the synthesis was performed in evacuated quartz ampules, which were dried at 1073 K under dynamic vacuum for several hours before usage. For the synthesis of AgBiSe₂, all the starting elements were thoroughly ground, sealed in ampules and annealed at 1123 K for 10 hours before cooling to room temperature. All procedures were carried out in horizontal tube furnaces with a heating rate of 2 K min⁻¹. The obtained powders were ground to a fine powder and consolidated into 0.7–1 mm thick, 12 mm diameter pellets at a force of 50 kN by pressing in steel dies at 473 K. The resulting discs were subsequently heated to 620 K in order to sinter the pellet and relax the microstructure. The resulting discs have more than 95% theoretical density, determined using a pycnometer.

Laboratory X-ray diffraction

Structural investigations were carried out by means of X-ray powder diffraction, using a PANalytical Empyrean powder diffractometer with CuK_α radiation ($\lambda_1 = 1.54056 \text{ \AA}$, $\lambda_2 = 1.54439 \text{ \AA}$) in Bragg–Brentano θ – 2θ geometry with a PIXcel detector with 255 measuring channels. Diffraction data were recorded in the 2θ range of 10° to 90° with a step size of 0.013° and a counting time of 40 s per step.

Synchrotron X-ray diffraction

X-ray total scattering data were collected at the 11-BM-B beam-line of the Advanced Photon Source at the Argonne National Laboratory. An incident photon energy of 29.90 keV ($\lambda = 0.414621 \text{ \AA}$) was employed. Samples were loaded into Kapton tubes and all scattering data were collected at room temperature. Due to the high X-ray absorption coefficient of the material, the powder was diluted with amorphous SiO₂ prior to any synchrotron measurements.

Rietveld analysis

Rietveld refinements were carried out using the GSAS II software.¹⁹ The average crystal structure of the vacancy-doped Ag_{1-x}BiSe₂ ($x = 0$ –7 mol%) was refined using the trigonal $P\bar{3}m1$ space group as a starting model. Fit indicators: R_{wp} , R_{exp} , and χ^2 were used to assess the quality of the refined structural models.²⁰ The following parameters were initially refined: (1) scale factor, (2) background coefficients, (3) peak shape, which was modeled using a modified Thomson–Cox–Hastings pseudo-Voigt function,²¹ (4) lattice constants, (5) fractional atomic coordinates, (6) isotropic atomic displacement parameters, and (7) zero-shift error. U_{iso} for Ag1 was fixed at a value of 0.075 in order to prevent unphysical values. Additionally, the presence of a minority (11.0–16.8%) $R\bar{3}m$ phase of AgBiSe₂ was included due to the existence of a strong shoulder on the diffraction maximum centered at a 2θ of ca. 11.35° . The values of R_{wp} were improved by approximately 1.5% upon the inclusion of the $R\bar{3}m$ phase. Trace amounts

(i.e., 1.7%) of the $R\bar{3}m$ structure of Bi₂Se₃ were also observed in Ag_{0.99}BiSe₂. Upon convergence, the fraction of Ag at Bi-sites, and *vice versa*, were then allowed to refine, but constrained to only allow sites with the same multiplicity to mix (i.e., Ag on Wyckoff site 1a for Bi1 on Wyckoff site 1b and Ag2 on Wyckoff site 2d for Bi2 on Wyckoff site 2d) and to achieve full occupancy at each site. Refinements without constraints on the occupancy in order to probe for the structural vacancy concentration yielded physically unreasonable values. Notably, site mixing between Ag1a and Bi1b yielded negligible occupancies for all compositions and was thus removed from the refinement. Furthermore, no site mixing was noted in the Ag_{0.95}BiSe₂ and Ag_{0.93}BiSe₂ compositions. It was not possible to obtain a stable refinement of the Ag occupancy and with it, the real Ag content. Therefore, all compositions given in this paper denote the nominal, synthetic composition.

Scanning electron microscopy

Microstructure images of the samples were obtained using a Merlin high-resolution scanning electron microscope (Carl Zeiss AG, Germany).

Transport measurements

The thermal diffusivity α was measured with a Linseis XFA 500 diffusivity instrument under vacuum. In order to maximize the emissivity, the samples were spray-coated with a thin layer of graphite before the measurement. Thermal conductivity values were determined using $\kappa = \alpha C_p d$, with C_p the heat capacity and d the geometric density. The heat capacity was estimated using the Dulong–Petit approximation and the theoretical densities were calculated from the molar mass and lattice parameters. The samples were cut into approximately 1 mm × 0.7 mm × 1 mm bars for electrical conductivity (σ) and Seebeck coefficient (S) measurements (Linseis LSR-3).

Speed of sound measurements were performed on consolidated discs using an Epoch 600 (Olympus) and 5 MHz transducers for longitudinal and transverse speeds of sound, respectively. The measurements were performed under nitrogen. The Grüneisen parameter and the Poisson ratio were calculated from the speed of sound data of AgBiSe₂ with:^{22,23}

$$\gamma = \frac{3}{2} \left(\frac{1 + \nu_p}{2 - 3\nu_p} \right); \quad \nu_p = \left(1 - 2 \left(\frac{\nu_{\text{trans}}}{\nu_{\text{long}}} \right)^2 \right) / \left(2 - 2 \left(\frac{\nu_{\text{trans}}}{\nu_{\text{long}}} \right)^2 \right). \quad (1)$$

The Debye temperature Θ_D , as well as the mean speed of sound ν_{mean} and the minimum lattice thermal conductivity κ_{min} , can be calculated using eqn (2)–(4).^{24–26}

$$\Theta_D = \frac{\hbar}{k_B} \left(\frac{6\pi^2}{V} \right)^{1/3} \cdot \nu_{\text{mean}} \quad (2)$$

$$\nu_{\text{mean}}^3 = \frac{3}{\nu_{\text{long}}^{-3} + 2\nu_{\text{trans}}^{-3}}, \quad (3)$$

$$\kappa_{\min} = \frac{1}{2} \left(\frac{\pi}{6} \right)^{\frac{1}{3}} k_B V^{\frac{2}{3}} (2\nu_{\text{trans}} + \nu_{\text{long}}). \quad (4)$$

Based on the model for point defect scattering,^{27–31} the lattice thermal conductivity of alloys was calculated using eqn (5)–(7) following Wang *et al.*²⁹

$$\frac{\kappa_{\text{L,alloy}}}{\kappa_{\text{L,pure}}} = \frac{\arctan(u)}{u}, \quad (5)$$

with $\kappa_{\text{L,alloy}}$ and $\kappa_{\text{L,pure}}$ the lattice thermal conductivities for the disordered alloy and the crystal without disorder, respectively. The disorder scaling parameter u can be calculated using the Debye temperature Θ_D , the volume per atom V , the mean speed of sound ν_{mean} as well as the scattering parameter Γ .

$$u^2 = \frac{\pi \Theta_D V}{2 h \nu_{\text{mean}}^2} \kappa_{\text{L,pure}} \Gamma; \quad (6)$$

The scattering parameter included the influence of the mass difference ΔM as well as the bonding force difference and strain field induced by point defects. Here, ΔM represents the mass difference between the two possible binary compounds and $a - a_{\text{pure}}$ the difference in lattice parameters.

$$\Gamma = x(1-x) \left[\left(\frac{\Delta M}{M} \right)^2 + \varepsilon \left(\frac{a - a_{\text{pure}}}{x a_{\text{pure}}} \right)^2 \right] \quad (7)$$

The parameter ε is related to elastic parameters such as the Grüneisen parameter and the Poisson ratio and may be calculated or used as a fitting parameter for the influence of strain. However, while the strain field has been shown to significantly affect the lattice thermal conductivity in some compounds,^{32–34} no change in the lattice parameter has been observed and no influence of the strain was included in the model.

3. Results and discussion

Structural characterization

An understanding of the crystal structures of AgBiSe_2 is important for gaining a deeper insight into the underlying structural influence on the transport. Known structures are shown in Fig. 1. AgBiSe_2 belongs to the I–V–VI₂ family of materials with I being Cu or Ag, the group V element Bi or Sb and VI denoting S, Se or Te. The ternary compound AgSbTe_2 , for instance, belongs to the family of TAGS (alloyed with GeTe) and LAST (alloyed with PbTe) thermoelectric materials that have shown remarkable zT values.^{35–39} While the compositions AgSbTe_2 and AgBiTe_2 crystallize in a cubic rock salt structure with full disorder of Ag and (Sb/Bi) on the crystallographic site, AgBiSe_2 is only stable in the rock salt structure (γ -phase, space group $Fm\bar{3}m$) above 580 K.⁶ Upon cooling, the Ag and Bi cations order, forming a mid-temperature rhombohedral phase (β -phase, space group $R\bar{3}m$). Below ~ 460 K, AgBiSe_2 crystallizes in a trigonal structure (α -phase, space group $P\bar{3}m1$) with two crystallographic sites for each of Ag and Bi. Whereas the cooling and phase transformation from the γ -phase corresponds to a transition with a large volume change and metal ordering, the phase transition between the β -phase and α -phase is only coupled to a slight atomic displacement and an elongation ($\alpha \rightarrow \beta$) of the unit cell in the z -direction.⁵

Fig. 2a shows a synchrotron diffraction pattern of AgBiSe_2 , representative of the fit quality and purity of all vacancy doped solid solutions $\text{Ag}_{1-x}\text{BiSe}_2$. The crystallographic data, obtained *via* Rietveld refinements against synchrotron diffraction data, can be found in the ESI.† With the exception of the sample with composition $\text{Ag}_{0.99}\text{BiSe}_2$ (1.7 wt% Bi_2Se_3), all samples remain phase pure up to a nominal vacancy concentration of $x = 0.05$. At $x = 0.07$ the solubility limit of Ag vacancies is exceeded and a minority impurity of 1.4 wt% Bi_4Se_3 is observed. Samples with even higher molar fractions of vacancies also exhibit secondary phases. This is as expected

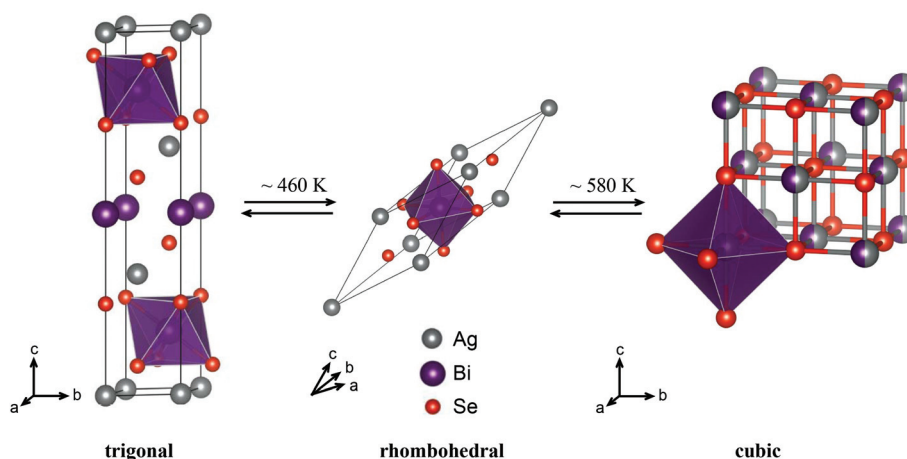


Fig. 1 Crystal structures of AgBiSe_2 with the occurring structural transformations. The high temperature NaCl structure in which Ag and Bi are disordered orders upon cooling into a rhombohedral phase and further into a trigonal phase at room temperature. Ag ions are shown in silver, Bi in purple and Se in red. Temperatures of the phase transition are based on literature values.⁶

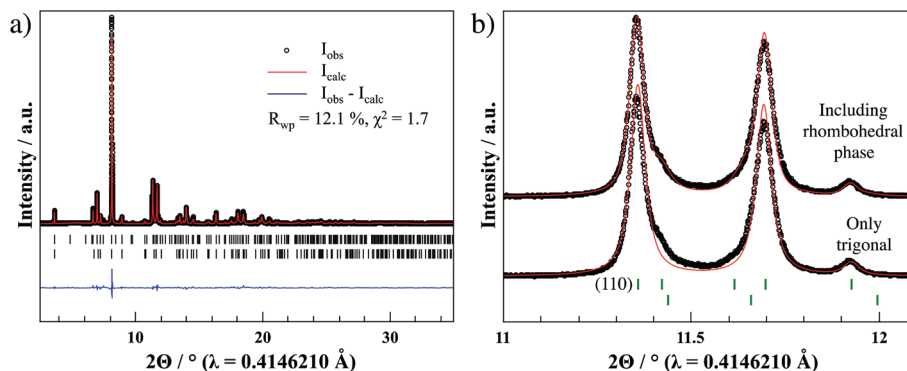


Fig. 2 (a) Representative Rietveld refinement of $\text{Ag}_{1-x}\text{BiSe}_2$ ($x = 0$ against synchrotron diffraction data. (b) Zoom on the (110) Miller reflection of AgBiSe_2 (trigonal phase), showing a shoulder at higher diffraction angles corresponding to the mid-temperature rhombohedral phase. Along with the trigonal room-temperature phase, a significant amount (~ 15 wt%) of the rhombohedral mid-temperature phase is required to achieve a better fit.

because in surpassing the solubility limit, phase segregation of bismuth selenide must occur in order to accommodate the loss of Ag.

Furthermore, all diffraction patterns show a significant amount of the rhombohedral phase of AgBiSe_2 to be present in all samples. Fig. 2b compares the Rietveld fits of the (110) Miller plane at a 2θ of 11.35° , with and without the additional rhombohedral phase. The rhombohedral phase exerts itself as a small shoulder on the higher angle side of the Bragg reflection and can easily be overlooked in laboratory X-ray diffraction with its lower $\Delta d/d$ resolution. The fraction of the rhombohedral phase is ~ 11 – 16 wt% in all samples and seems to be independent of the vacancy concentration. The respective fractions of the rhombohedral phase can be found in the crystallographic data in the ESI.† These data suggest that when the material is cooled down from the reaction temperature of the high temperature rock salt phase with full Ag and Bi disorder, a significant fraction of the sample is frozen in the mid-temperature range and does not fully transform into the trigonal room temperature phase.

In addition to the two AgBiSe_2 phases, significant anti-site disorder can be found between Ag and Bi on their respective sites. While no disorder seems to occur on the Ag 1a and Bi 1b Wyckoff positions (see the Experimental section), a certain amount of anti-site disorder between the Ag 2d and Bi 2d positions can be observed. For instance, the vacancy free sample of AgBiSe_2 exhibits a disorder of $6.0(1)\%$ Ag on the Bi 2d site and *vice versa*. With increasing the vacancy concentration, the disorder decreases (see Fig. 3), resulting in no observable anti-site disorder in the samples with compositions $\text{Ag}_{0.95}\text{BiSe}_2$ and $\text{Ag}_{0.93}\text{BiSe}_2$. The vacancy concentration dependent anti-site disorder can be understood considering the phase transformations and different structures. At high temperatures in the rock salt structure type all Bi and Ag are distributed and disordered over one crystallographic site. During cooling, the metal ions need to order into the respective low temperature Wyckoff positions. Anti-site disorder can occur when the ordering is not fast enough with respect to the cooling rate. In

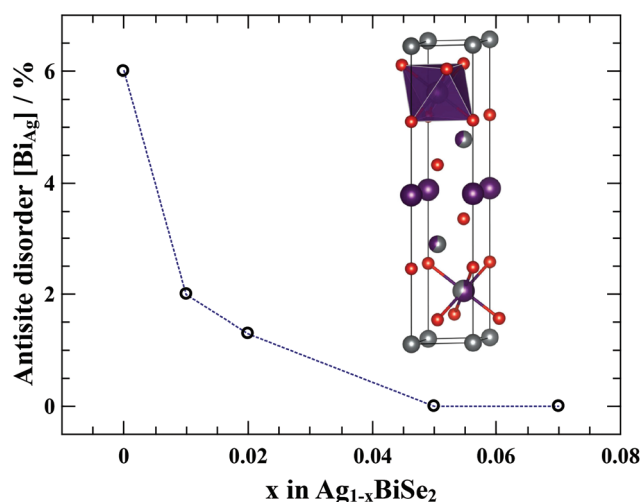


Fig. 3 Resulting anti-site disorder on the Bi 2d and Ag 2d crystallographic sites. The inset shows the two sites, with an arbitrary 40% disorder for better visibility. With increasing the amount of vacancies in the structure, the amount of anti-site disorder decreases, suggesting an influence of the vacancies on the ordering of Ag^+ and Bi^{3+} during the phase transitions.

other words, if the atomic diffusion coefficients of Ag^+ and Bi^{3+} are not high enough, anti-site disorder occurs. With increasing the vacancy concentration, more pathways are possible due to vacant or interstitial sites and full ordering of the metals can occur faster. A similar behavior has recently been found in AgBiS_2 ,^{40,41} in which the Ag vacancy concentration significantly affects the order–disorder in the structure.

Chemical stability of vacancy doping

The synchrotron diffraction data show that a certain amount of Ag vacancies seems possible in AgBiSe_2 , as no large fraction of segregated phases can be found in the diffraction patterns. However, thermodynamically speaking, the introduction of vacancies and holes may not be energetically favorable and a

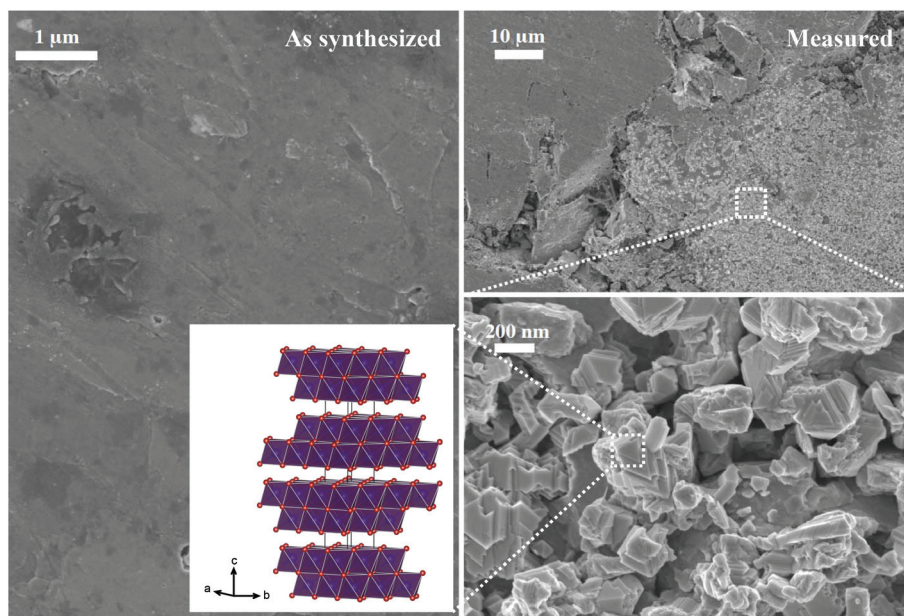


Fig. 4 Scanning electron micrographs of the synthesized AgBiSe_2 ($x = 0.05$ phase pure, left) and of a pellet after multiple measurement runs. The impurity phase crystallizes in a trigonal plate crystal habit, indicative of Bi_2Se_3 . During the measurements Bi_2Se_3 segregates out in order to compensate for the vacancies in the structure, leading to more Bi_2Se_3 and a lower vacancy concentration in the structure.

segregation of $\text{Ag}_{1-x}\text{BiSe}_2$ into bismuth selenide and vacancy-free AgBiSe_2 is possible. Fig. 4 and 5 show scanning electron micrographs (SEM) and laboratory X-ray diffraction patterns for vacancy doped samples before and after multiple measurement runs. In the vacancy doped samples, a significant amount of the secondary phase Bi_2Se_3 can be found as seen in the plate-like crystal habit in the SEM (Fig. 4) and the additional Bragg reflections in the diffraction pattern (Fig. 5). In other words, while vacancies exhibit a certain solubility

limit in AgBiSe_2 in solid-state synthesis, this solubility seems to be only kinetically stable. With multiple measurement cycles, compensating phase segregation occurs that leaves formally undoped AgBiSe_2 and Bi_2Se_3 behind. The occurring phase segregation leads to a large hysteresis in the thermoelectric transport of the vacancy doped samples. With repeated cycling a thermodynamically stable phase forms, which affects significantly the thermoelectric properties together with the secondary phase. The vacancy-free sample does also show a small degree of hysteresis, due to the first-order phase transition or the herein found anti-site disorder; however, no sample decomposition (*i.e.* no phase segregation) is apparent as seen in the vacancy doped samples. Interestingly, halogen doping for Se removes the hysteresis from the thermoelectric transport data entirely.⁶

Thermoelectric transport

Fig. 6 shows the thermoelectric transport properties of the vacancy doped $\text{Ag}_{1-x}\text{BiSe}_2$. Due to the occurring phase segregation, forming Bi_2Se_3 upon cycling, only heating data are shown here. All Seebeck coefficients are negative, suggesting electrons as the majority charge carriers. The increase of thermopower with temperature suggests lightly doped transport with a maximum of the Seebeck coefficient at around 600 K, due to carrier excitation across the band gap of ~ 0.6 eV.⁶ With increasing the vacancy concentration, the intrinsically n-type doped Seebeck coefficient of the undoped sample increases up to $x = 0.05$ and then decreases again. This may be due to the introduction of holes through the vacancies, which is expected to lower the electron carrier concentration in the system. However, in the absence of Hall data, providing carrier mobi-

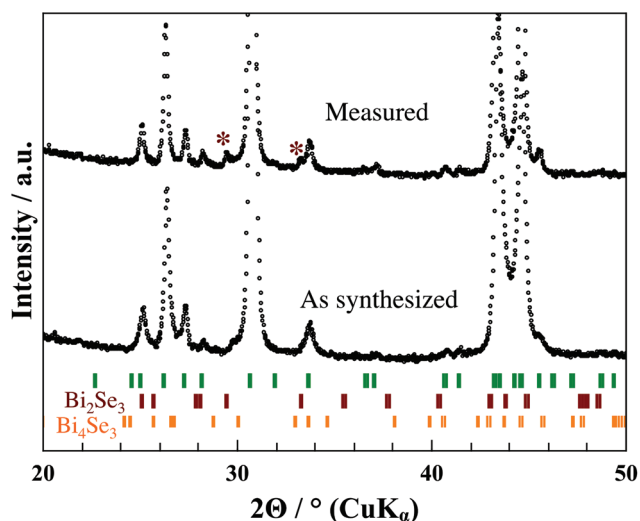


Fig. 5 Laboratory X-ray diffraction of an as-synthesized AgBiSe_2 (including a minor fraction of Bi_4Se_3) before and after multiple measurement runs, showing Bi_2Se_3 segregating as an impurity phase.

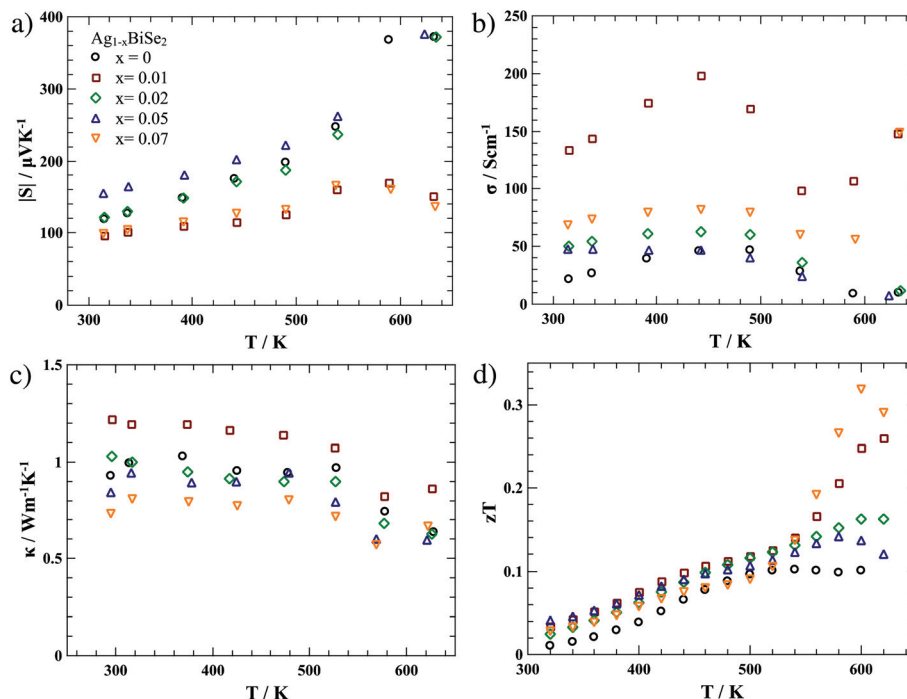


Fig. 6 Thermoelectric transport properties of $\text{Ag}_{1-x}\text{BiSe}_2$ during heating. (a) Seebeck coefficients, (b) electrical conductivity, (c) thermal conductivity and (d) figure of merit zT .

lity and carrier densities, this is only speculative. The vacancies and anti-site disorder may affect the carrier mobility and the scattering mechanism, as well as introduce novel band features, in the event that the anti-site disorder disrupts a rigid band approximation. A crossover into a fully p-type doped system does not occur as has been shown when doping with Pb.⁵ At a vacancy composition of $x = 0.07$, the Seebeck coefficient decreases again, possibly due to the formation of the compensating secondary phase (see above). A similar situation has been found in other chalcopyrites such as $\text{Cu}_2\text{ZnGeSe}_4$ in which a segregated minority phase affects the transport properties without being visible using X-ray diffraction.⁴² While vacancies may lead to p-type transport in solution synthesized AgBiSe_2 ,⁸ synthetically induced defects during solid-state synthesis do not lead to hole dominated transport.

As shown in some recent studies on AgBiSe_2 ,^{5,6} electrical and thermal conductivities are highly influenced by the phase transitions around 460 K and 580 K. Specifically, thermal conductivity exhibits some interesting trends. First, no Umklapp-scattering is visible that would result in a T^{-1} dependence of thermal conductivity. The temperature independence of thermal conductivity has previously been observed.^{4,6} Second, no trend in thermal conductivity with composition seems obvious (Fig. 6c), unless the anti-site disorder and vacancies are considered.

Influence of vacancies and anti-site disorder

Fig. 7 shows the lattice thermal conductivity at 325 K as a function of x in $\text{Ag}_{1-x}\text{BiSe}_2$, including a 5% measurement un-

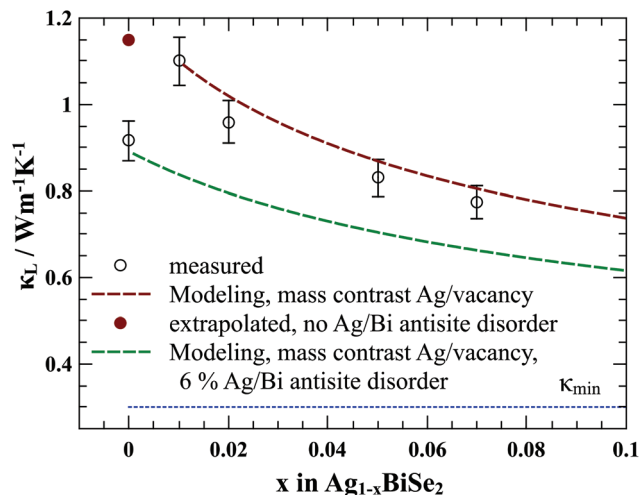


Fig. 7 Lattice thermal conductivity κ_L of $\text{Ag}_{1-x}\text{BiSe}_2$ against the synthetic vacancy concentration, including a 5% measurement uncertainty. The red dotted line corresponds to the modeled influence of point defect scattering due to Ag vacancies starting at $\text{Ag}_{0.99}\text{BiSe}_2$, which reduces the lattice thermal conductivity. Extrapolating the modeled influence, a value for the lattice thermal conductivity at $x = 0$ is extracted, which deviates from the measured data. Introducing a 6% Ag–Bi anti-site disorder lowers the lattice thermal conductivity (green line) at $x = 0$ significantly and describes the measured data well.

certainty. The lattice thermal conductivity κ_L was calculated by subtracting the electronic contribution to the total thermal conductivity using the Wiedemann–Franz law, and the Lorenz number was calculated from the measured Seebeck coefficient.

cients.⁴³ The undoped AgBiSe₂ exhibits a low lattice thermal conductivity, which increases for $x = 0.01$ in the vacancy doped samples. Then, with the increase of Ag deficiency, κ_L decreases. Anti-site disorder as well as the introduction of vacancies can act as point defects with respect to the thermal conductivity of a perfect lattice,^{18,29,44} so the influence of point defect scattering on lattice thermal conductivity was assessed using the equations given by Wang *et al.* (see the Experimental section).²⁹

The measured speeds of sound in AgBiSe₂ are used to calculate the necessary parameters for the point defect modeling. All the parameters obtained from speed of sound measurements are given in Table 1. It needs to be mentioned that the longitudinal speed of sound is lower by $\sim 100 \text{ m s}^{-1}$ in the vacancy doped samples, compared to the vacancy-free material. No influence on the transverse speeds of sound can be observed. A Debye temperature θ_D of 138 K and a Grüneisen parameter of $\gamma = 1.6$ are obtained for AgBiSe₂. While the obtained Grüneisen parameter is slightly lower than the literature value of $\gamma = 2.9$ (ref. 45) (obtained from thermal expansion measurements), the values are within the statistical scatter of the lattice thermal conductivity as a function of γ .³² The extracted Debye temperature is close to the literature value of 135 K,⁴ suggesting that above room temperature, Umklapp scattering and the T^{-1} dependence of the lattice thermal conductivity should be prevalent. Umklapp scattering cannot be observed in the data, which hints at either a large degree of disorder or a large anharmonicity.⁴ Indeed, the large Grüneisen parameter shows that the material exhibits a high anharmonicity of lattice vibrations, possibly due to the 6s² lone pair of Bi³⁺.^{4,32,45}

Fig. 7 shows the results of modeling the influence of point defects on the thermal conductivity. First, the lattice thermal conductivity of Ag_{0.99}BiSe₂, with only a small amount of Ag–Bi anti-site disorder, was used as the starting value to assess the influence of the vacancies on κ_L . Here, the mass contrast of eqn (7) corresponds to the difference in mass of the two compounds AgBiSe₂ and a hypothetical V_{Ag}BiSe₂ with a 100% Ag vacancy V_{Ag}. As seen in Fig. 7 (red line), with increasing the amount of Ag vacancies, the lattice thermal conductivity is reduced due to point defect scattering with the maximum amount of mass contrast possible, *i.e.* the mass difference is the atomic mass of Ag. A similar behavior of vacancies in the thermal conductivity has been found in vacancy doped SnTe.¹⁸ The modeled influence of vacancies, starting with the compound Ag_{0.99}BiSe₂, is extrapolated to $x = 0$ to estimate the

lattice thermal conductivity of a vacancy-free AgBiSe₂. The extracted value is much higher than the experimentally observed lattice thermal conductivity of the undoped sample. However, the Rietveld refinements of the synchrotron diffraction data show a 6.0(1)% Bi–Ag anti-site disorder in AgBiSe₂. Using the extrapolated value for a vacancy and disorder free AgBiSe₂ as the input, a 6% disorder and its corresponding mass contrast are used to calculate the influence on the thermal conductivity (green line). This anti-site disorder significantly lowers the thermal conductivity of the undoped AgBiSe₂ and leads to a value within the measurement uncertainty of the observed lattice thermal conductivity for $x = 0$. It should be mentioned, however, that the samples of $x = 0.01$ and 0.02 exhibit a small amount of Ag–Bi anti-site disorder as well, which is expected to lower the lattice thermal conductivity already compared to a fully ordered structure of Ag_{0.99}BiSe₂ and Ag_{0.98}BiSe₂. In addition, the influence of the rhombohedral secondary phase is expected to affect the overall lattice thermal conductivity due to enhanced grain boundary scattering. Since the fraction of the secondary phase is more or less constant, the changes observed in κ_L with decreasing Ag content can be assumed to derive solely (*i.e.* within experimental uncertainty) from the observed point defect scattering. The influence of grain boundary scattering was therefore not included in the modeling of the lattice thermal conductivity.

These data show that in the case of the undoped AgBiSe₂, the observed anti-site disorder leads to enhanced point defect scattering. When introducing Ag vacancies, the anti-site disorder is diminished, which increases κ_L . Further increases in the Ag vacancy concentration provide point defect scattering due to the maximum possible mass contrast and reduce the lattice thermal conductivity κ_L .

4. Conclusion

In conclusion, we have used a combination of synchrotron diffraction and transport measurements to elucidate the effect of vacancy doping in Ag_{1-x}BiSe₂ on the structural and thermoelectric properties. Rietveld refinements show a certain synthetic solubility limit of Ag vacancies in the structure as well as a Bi–Ag anti-site disorder. With increasing the vacancy concentration, the degree of anti-site disorder decreases, possibly due to open diffusion pathways for an easier metal ordering during cooling. The vacancies and anti-site disorder lead to enhanced point defect scattering of phonons, severely influencing the lattice thermal conductivity in Ag_{1-x}BiSe₂. This study highlights the importance of anti-site disorder and the influence of vacancy doping on the structure of thermoelectric materials, hopefully allowing for a deeper understanding of the associated structural influences on thermoelectrics.

Conflict of interest

The authors declare no competing financial interests.

Table 1 Elastic properties obtained via speed of sound measurements on AgBiSe₂. Longitudinal and transverse speeds of sound, v_{long} and v_{trans} , the mean speed of sound v_{mean} , Debye temperature θ_D , Grüneisen parameter γ , Poisson ratio ν_P and glassy limit of the thermal conductivity κ_{min} are provided

$v_{\text{long}}/\text{ms}^{-1}$	$v_{\text{trans}}/\text{ms}^{-1}$	$v_{\text{mean}}/\text{ms}^{-1}$	θ_D/K	γ	ν_P	$\kappa_{\text{min}}/\text{WmK}^{-1}$
2161	1222	1358	138	1.6	0.265	0.30

Acknowledgements

We gratefully acknowledge the financial support through start-up funding provided by the Justus-Liebig-University Giessen as well as the support from the Funds of the Chemical Industry (FCI). Furthermore, we acknowledge financial support provided by the DFG via the GRK (research training group) 2204 "Substitute Materials for sustainable Energy Technologies". The authors acknowledge the use of the Advanced Photon Source at the Argonne National Laboratory for the synchrotron diffraction data, as supported by the U.S. Department of Energy, Office of Science, Office of Basic Energy Sciences, under contract no. DE-AC02-06CH11357.

References

- W. G. Zeier, J. Schmitt, G. Hautier, U. Aydemir, Z. M. Gibbs, C. Felser and G. J. Snyder, *Nat. Rev. Mater.*, 2016, 16032.
- G. J. Snyder and E. S. Toberer, *Nat. Mater.*, 2008, 7, 105–114.
- E. S. Toberer, A. Zevalkink and G. J. Snyder, *J. Mater. Chem.*, 2011, 21, 15843–15852.
- D. T. Morelli, V. Jovovic and J. P. Heremans, *Phys. Rev. Lett.*, 2008, 101, 35901.
- L. Pan, D. Be and N. Dragoe, *J. Am. Chem. Soc.*, 2013, 135, 4914–4917.
- S. N. Guin, V. Srihari and K. Biswas, *J. Mater. Chem. A*, 2015, 3, 648–655.
- C. Xiao, J. Xu, B. Cao, K. Li, M. Kong and Y. Xie, *J. Am. Chem. Soc.*, 2012, 134, 7971–7977.
- C. Xiao, X. Qin, J. Zhang, R. An, J. Xu, K. Li, B. Cao, J. Yang, B. Ye and Y. Xie, *J. Am. Chem. Soc.*, 2012, 134, 18460–18466.
- D. Parker, A. F. May and D. J. Singh, 2015, arXiv, 3379, 1–10.
- T. Zhu, L. Hu, X. Zhao and J. He, *Adv. Sci.*, 2016, 3, 1600004.
- Z. Li, C. Xiao, H. Zhu and Y. Xie, *J. Am. Chem. Soc.*, 2016, 138, 14810–14819.
- G. Jiang, J. He, T. Zhu, C. Fu, X. Liu, L. Hu and X. Zhao, *Adv. Funct. Mater.*, 2014, 24, 3776–3781.
- A. Zevalkink, W. G. Zeier, E. Cheng, G. J. Snyder, J.-P. Fleurial and S. Bux, *Chem. Mater.*, 2014, 26, 5710–5717.
- G. S. Pomrehn, A. Zevalkink, W. G. Zeier, A. van de Walle and G. J. Snyder, *Angew. Chem., Int. Ed.*, 2014, 53, 3422–3426.
- T. W. Day, K. S. Weldert, W. G. Zeier, B.-R. Chen, S. L. Moffitt, U. Weis, K. P. Jochum, M. Panthöfer, M. J. Bedzyk, G. J. Snyder and W. Tremel, *Chem. Mater.*, 2015, 27, 7018–7027.
- W. G. Zeier, S. Anand, L. Huang, H. Ran, H. Zhang, Z. Ren, C. Wolverton and G. J. Snyder, *Chem. Mater.*, 2017, 29, 1210–1217.
- M. H. Lee, D.-G. Byeon, J.-S. Rhyee and B. Ryu, *J. Mater. Chem. A*, 2017, 5, 2235–2242.
- G. Tan, W. G. Zeier, F. Shi, P. Wang, G. J. Snyder, V. P. Dravid and M. G. Kanatzidis, *Chem. Mater.*, 2015, 27, 7801–7811.
- B. H. Toby and R. B. Von Dreele, *J. Appl. Crystallogr.*, 2013, 46, 544–549.
- R. A. Young, *The Rietveld Method*, Oxford University Press, New York, 1993.
- P. Thompson, D. E. Cox and J. B. Hastings, *J. Appl. Crystallogr.*, 1987, 20, 79–83.
- L.-D. Zhao, J. He, D. Berardan, Y. Lin, J.-F. Li, C.-W. Nan and N. Dragoe, *Energy Environ. Sci.*, 2014, 7, 2900–2924.
- D. S. Sanditov and V. N. Belomestnykh, *Tech. Phys.*, 2011, 56, 1619–1623.
- A. F. May and G. J. Snyder, in *Thermoelectrics Handbook: Thermoelectrics and its Energy Harvesting*, ed. D. M. Rowe, CRC Press, Boca Raton, 2012.
- A. Zevalkink, E. S. Toberer, W. G. Zeier, E. Flage-Larsen and G. J. Snyder, *Energy Environ. Sci.*, 2011, 4, 510–518.
- O. L. Anderson, *J. Phys. Chem. Solids*, 1963, 24, 909–917.
- G. Alekseeva, B. Efimova, L. M. Ostrovsk, O. S. Serebrya and M. Tsy-pin, *Sov. Phys. Semicond.*, 1971, 4, 1122.
- P. G. Klemens, *Proc. Phys. Soc.*, 1955, 68, 1113–1128.
- H. Wang, J. Wang, X. Cao and G. J. Snyder, *J. Mater. Chem. A*, 2014, 2, 3169–3174.
- J. Callaway and H. C. Baeyer, *Phys. Rev.*, 1960, 126, 1149–1154.
- J. Callaway, *Phys. Rev.*, 1959, 111, 1046–1051.
- W. G. Zeier, A. Zevalkink, Z. M. Gibbs, G. Hautier, M. G. Kanatzidis and G. J. Snyder, *Angew. Chem., Int. Ed.*, 2016, 55, 6826–6841.
- W. G. Zeier, Y. Pei, G. Pomrehn, T. Day, N. A. Heinz, C. P. Heinrich, G. J. Snyder and W. Tremel, *J. Am. Chem. Soc.*, 2013, 135, 726–732.
- C. P. Heinrich, T. W. Day, W. G. Zeier, G. J. Snyder and W. Tremel, *J. Am. Chem. Soc.*, 2014, 136, 442–448.
- B. Poudel, Q. Hao, Y. Ma, Y. Lan, A. Minnich, B. Yu, X. Yan, D. Wang, A. Muto, D. Vashaee, X. Chen, J. Liu, M. S. Dresselhaus, G. Chen and Z. Ren, *Science*, 2008, 320, 634–638.
- K. Biswas, J. He, Q. Zhang, G. Wang, C. Uher, V. P. Dravid and M. G. Kanatzidis, *Nat. Chem.*, 2011, 3, 160–166.
- K. F. Hsu, S. Loo, F. Guo, W. Chen, J. S. Dyck, C. Uher, T. Hogan, E. K. Polychroniadis and M. G. Kanatzidis, *Science*, 2004, 303, 818–821.
- D. Wu, L. D. Zhao, S. Hao, Q. Jiang, F. Zheng, J. W. Doak, H. Wu, H. Chi, Y. Gelbstein, C. Uher, C. Wolverton, M. Kanatzidis and J. He, *J. Am. Chem. Soc.*, 2014, 136, 11412–11419.
- K. F. Hsu, S. Loo, F. Guo, W. Chen, J. S. Dyck, C. Uher, T. Hogan, E. K. Polychroniadis and M. G. Kanatzidis, *Science*, 2004, 303, 818–821.
- S. N. Guin and K. Biswas, *Chem. Mater.*, 2013, 25, 3225–3231.
- S. N. Guin, S. Banerjee, D. Sanyal, S. K. Pati and K. Biswas, *Inorg. Chem.*, 2016, 55, 6323–6331.

- 42 W. G. Zeier, A. LaLonde, Z. M. Gibbs, C. P. Heinrich, M. Panthöfer, G. J. Snyder and W. Tremel, *J. Am. Chem. Soc.*, 2012, **134**, 7147–7154.
- 43 H.-S. Kim, Z. M. Gibbs, Y. Tang, H. Wang and G. J. Snyder, *APL Mater.*, 2015, **3**, 41506.
- 44 B. R. Ortiz, H. Peng, A. Lopez, P. a. Parilla, S. Lany and E. S. Toberer, *Phys. Chem. Chem. Phys.*, 2015, **17**, 19410–19423.
- 45 M. D. Nielsen, V. Ozolins and J. P. Heremans, *Energy Environ. Sci.*, 2013, **6**, 570–578.